Analyst

RSC Publishing

PAPER

View Article Online
View Journal

Cite this: DOI: 10.1039/c3an01219k

A quartz enhanced photo-acoustic gas sensor based on a custom tuning fork and a terahertz quantum cascade laser

Pietro Patimisco,[ab] Simone Borri,[b] Angelo Sampaolo,[a] Harvey E. Beere,[c] David A. Ritchie,[c] Miriam S. Vitiello,[d] Gaetano Scamarcio[ab] and Vincenzo Spagnolo*[ab]

Received 21st June 2013
Accepted 3rd October 2013

DOI: 10.1039/c3an01219k

www.rsc.org/analyst

An innovative quartz enhanced photoacoustic (QEPAS) gas sensing system operating in the THz spectral range and employing a custom quartz tuning fork (QTF) is described. The QTF dimensions are 3.3 cm × 0.4 cm × 0.8 cm, with the two prongs spaced by ~800 μm. To test our sensor we used a quantum cascade laser as the light source and selected a methanol rotational absorption line at 131.054 cm^{-1} (~3.93 THz), with line-strength $S = 4.28 \times 10^{-21}$ cm mol^{-1}. The sensor was operated at 10 Torr pressure on the first flexion QTF resonance frequency of 4245 Hz. The corresponding *Q*-factor was 74 760. Stepwise concentration measurements were performed to verify the linearity of the QEPAS signal as a function of the methanol concentration. The achieved sensitivity of the system is 7 parts per million in 4 seconds, corresponding to a QEPAS normalized noise-equivalent absorption of 2×10^{-10} W cm^{-1} $Hz^{-1/2}$, comparable with the best result of mid-IR QEPAS systems.

Introduction

High sensitivity THz molecular spectroscopy is a powerful tool both for laboratory purposes and for remote sensing. Many absorption and emission molecular lines of large interest fall in this spectral region, where typical absorption strengths are of the same order of magnitude of those observed in the mid-IR and from three to six orders of magnitude stronger than those measured in the microwave region. For example, gas species such as water, nitrogen compounds, oxygen, and chlorine present strong absorption bands in the TH spectral range. The precise knowledge of their concentrations in the stratosphere and upper troposphere areas is crucial for the study of chemical processes related to ozone depletion, pollution monitoring, and global warming.[1] Other important applications include direct detection of traces of such gases in open air[2,3] and spectroscopic identification of explosives[4] and different crystalline polymorphic states of drugs.[5]

In the last few years, the rapid growth of new technologies needed to access this region is stimulating a resurgence in THz spectroscopic application. A number of THz sensing systems using different optical techniques have been employed for gas sensing. Bigourd *et al.*[6] reported a sensor based on photomixing techniques in the range 0.5–1.5 THz to detect and quantify small quantities of hydrogen cyanide, carbon monoxide, formaldehyde, and water. The achieved detection limits for HCN, CO, and H_2CO were 9 parts in 10^6 (ppm), 0.1% and 114 ppm respectively. A broadband trace gas sensor at 0.5 THz based on chirped-pulse THz absorption spectroscopy has been demonstrated to detect OCS, N_2O, and methanol (CH_3OH) with noise equivalent concentration of a few hundreds of ppm in volume.[7] Methylchloride detection in the ppm range with long-baseline THz spectroscopy based on a white cell design has been also reported.[8] Nevertheless, the THz region of the electromagnetic spectrum is still largely unexplored, due to limited options for optical components, detectors and tunable and powerful coherent sources.

The sensitivity of any spectroscopic technique is ultimately limited by the available optical power and, in these terms, quantum cascade lasers (QCLs) represent the most promising THz light source. Since their first demonstration,[9] their optical performance improved dramatically.[10,11] THz QCLs can provide single-mode emission[11] and with output powers up to 138 mW in continuous wave operation at cryogenic temperatures.[12] To date, THz QCLs have been employed for high resolution molecular spectroscopy, exploiting their high frequency stability and spectral purity[13] and applications to trace gas detection have been limited to direct absorption[14,15] or amplitude modulation spectroscopy, with detectable absorption, α_{min}, in the 10^{-6} cm^{-1} $Hz^{-1/2}$ range.[16] Improvement of such

[a]*Dipartimento Interateneo di Fisica, Università e Politecnico di Bari, Via Amendola 173, I-70126 Bari, Italy. E-mail: v.spagnolo@poliba.it*

[b]*IFN-CNR UOS Bari, via Amendola 173, 70126 Bari, Italy*

[c]*Cavendish Laboratory, University of Cambridge, J. J. Thomson Avenue, Cambridge CB3 0HE, UK*

[d]*NEST, CNR-Istituto Nanoscienze and Scuola Normale Superiore, Piazza San Silvestro 12, I-56127 Pisa, Italy*

detection sensitivities requires upgrading to more performing spectroscopic techniques.

Among the most robust and sensitive trace-gas detection techniques, quartz-enhanced photo-acoustic spectroscopy (QEPAS) is capable of recording sensitivities with a compact and relatively low-cost acoustic detection module (ADM). The key innovation of this method is to invert the common photo-acoustic approach[17] and accumulate the acoustic energy in a sharply resonant quartz tuning fork (QTF) with a very high quality factor, which acts as a piezoelectric acoustic transducer. In combination with mid-infrared (mid-IR) QCLs, the QEPAS technique has proven to offer the advantage of high selectivity and fast time-response. Very efficient QCL-based QEPAS sensors have been demonstrated for trace detection of several chemical species, such as NH_3, NO, CO_2, N_2O, CO, CH_2O, *etc.*[18–21] Very recently, a record detection limit of 50 parts per trillion has been reported for SF_6,[22] corresponding to a normalized noise equivalent absorption (NNEA) value of 2.7×10^{-10} W cm^{-1} Hz$^{-1/2}$, in strong competition with the best reported values obtained using highly sensitive techniques, such as cavity ring-down spectroscopy and off-axis integrated cavity output spectroscopy, characterized by very long optical path-lengths.[23] One of the main advantages of the QEPAS techniques is that no optical detection is required, allowing to avoid the use of low-noise but expensive, bulky and cryogenic bolometric THz detectors. Moreover, mainly rotational levels are involved in THz absorption processes and rotational–translational (R–T) relaxation rates are up to three orders of magnitude faster with respect to vibrational–translational (V–T) one.[24] The QEPAS signal strongly depends on the energy relaxation rates of the absorption gas species and the possibility to work with fast relaxing transition levels allows to operate at low pressure, so taking advantage of the typically very high QTF *Q*-factors and enhancing the selectivity of the QEPAS sensor systems.

To date, all the QEPAS sensors reported in the literature exploit "standard" QTFs, optimized for timing applications, such as those used in clock watches. These QTFs have a resonance frequency of ~32.76 kHz and are characterized by a very small sensitive volume between their prongs (~0.3 × 0.3 × 3 mm^3). QEPAS sensors operating in the spectral wavelength range 1–10 μm have been demonstrated.[17,21] The extension of the QEPAS technique into the THz spectral region (λ > 30 μm) has been delayed, mainly due to the lack of affordable CW laser sources and the difficulty of a suitable focalization of the long-wavelength laser beam between the prongs (300 μm) of the standard QTF. Indeed, the laser beam has not to hit the QTF, otherwise an undesirable non-zero background arises and can be several times larger than the thermal noise level of the QEPAS sensor, so strongly limiting the final detection sensitivity.[21,25] Thus the use of QTFs with larger prong spacing is mandatory to extend the QEPAS operation in the THz range. Very recently we reported on the first demonstration of a QEPAS sensor operating in the THz range, employing a custom QTF.[26] We will report here a detailed description of the design and characterization of this innovative THz optoacoustic sensor and the related custom size QTF sensing module.

Custom quartz tuning fork

In order to focus the THz beam between the two prongs of the QTF without illuminating it, we employed for our experiments a tuning fork having the same geometry of the standard one, but about 6 times bigger. Starting from z-cut quartz wafer, standard photolithographic techniques were used to etch the QTF.[27] A 600/2000 Å chromium/gold layer was deposited on both sides of the QTF for electrical contacts. The QTF dimensions are 3.3 cm × 0.4 cm, with a thickness of 0.8 mm; each prong is 17.7 mm long and 1.4 mm wide. The prongs are separated by a gap of ~800 μm. The schematic of the QTF resonator employed in this work is shown in Fig. 1. In order to employ this custom QTF in a QEPAS sensing system we have to verify that it behaves like a standard tuning fork transducer in terms of resonance frequency and quality factor.

1. QTF simplified theoretic vibrational model. The basic principle of the tuning fork is well known: two prongs connected at one end make a resonator, whose resonance frequencies are defined by the properties of the composing material and by its geometry.

The resonator is fixed on a holder structure. The available resonance frequencies of the tuning fork can be found analytically by considering one arm of the fork as a cantilever vibrating prong. In the fundamental flexural mode of oscillation, the tines move in opposite directions and the centre-of-mass of the fork remains unchanged. This flexural mode vibration can be modelled by considering that each arm of the tuning fork behaves as a clamped prong. In this approximation, the frequency of the vibration modes is obtained by including a free-motion condition on one boundary of the prong and a clamped condition on the other (clamped-free boundary condition) and then solving for the propagation of the shear acoustic wave. Assuming the elastic Young modulus E of the composing material, the moment of inertia I of the prong and the cross-sectional area $A = T \cdot y$ are constant along the prong length, and the free motion is then given by the following fourth-order differential equation according to the classical Euler–Bernoulli theory:

$$EI\frac{\partial^4 y}{\partial x^4}(x,t) + \rho A\frac{\partial^4 y}{\partial t^4}(x,t) = 0 \qquad (1)$$

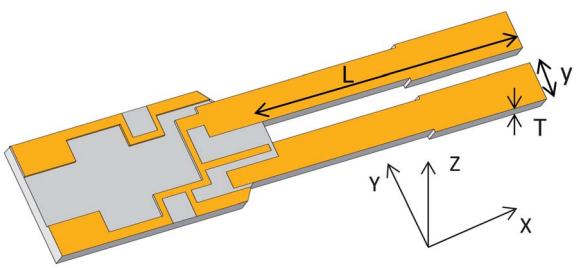

Fig. 1 Schematic of the employed quartz crystal tuning-fork resonator. The two prongs are oriented along the *X* quartz crystallographic axis. The yellow areas mimic the gold pattern used for electrical contacts. $L = 17.7$ mm, $y = 1.4$ mm and $T = 0.8$ mm.

where ρ is the density of the material, t is the time and x and y are directions represented in Fig. 1. Eqn (1) can be solved by imposing boundary conditions for the supports of the cantilever prong, and we can calculate the eigenfrequencies f_n given by:[28]

$$f_n = \frac{\pi K}{8L^2}\sqrt{\frac{E}{\rho}}n^2 \quad (2)$$

where $K = \sqrt{(I/A)}$ is the radius of gyration of the prong cross-section, that for a bar with rectangular cross-section is equal to $1/\sqrt{12}$ times the thickness.

When the tuning fork undergoes harmonic oscillations of small amplitude in a fluid, it tends to induce particles motion in the fluid which gives rise to energy loss and additional inertia. Since the molecular mean free path is much smaller than the characteristic length of the structure, the gas behaves entirely as a continuous fluid. Under these conditions, eqn (1) becomes:[28]

$$EI\frac{\partial^4 y}{\partial x^4}(x,t) + C_d\frac{\partial y}{\partial t}(x,t) + (\rho A + u)\frac{\partial^4 y}{\partial t^4}(x,t) = 0 \quad (3)$$

where C_d is the damping parameter and u the added mass per unit length. For vibration in gases the damping remains sufficiently low so that the second term of eqn (3) can be neglected. Then for the resonant frequencies one gets:

$$f_n' = \frac{\pi}{8L^2}\sqrt{\frac{EI}{(\rho A + u)}}n^2 \quad (4)$$

Since $u \ll \rho A$, combing eqn (2) and (3), in a first approximation the frequency shift Δf due to gas is given by:

$$\Delta f = \frac{f_n - f_n'}{f_n'} = -\frac{1}{2}\frac{u}{\rho A} \quad (5)$$

The added mass is proportional to the density ρ_0 of the fluid medium. Since the relationship between the pressure P and the density ρ_0 in a gas is $P \propto \rho_0$ we can easily get that Δf should vary linearly with the gas pressure. In addition, the fluid damping influences negatively the quality factor Q of the flexural mode. In fact, the reaction force due to the presence of the gas acting on the vibrating body leads to energy dissipation by acoustic losses. Assuming that the fluid drag force is the dominant damping source, *i.e.* the resonator is isolated from other objects so the other damping effects are not considered, the fluid damping parameter can be expressed as: $C_d \propto \sqrt{(\rho_0 f_n \mu)}$ where μ is the viscosity of the fluid.[29] Using the relationship $P \propto \rho_0$, we can express the dependence of the damping parameter with the gas pressure as: $C_d \propto \sqrt{P}$. So, the influence of the fluid damping on Q can be expressed in terms of the energy loss $1/Q(P)$ at the gas pressure P: $C_d = 1/(Q(P) - 1/Q_0)$ where Q_0 is the tuning fork Q factor under vacuum, which depends only on internal losses and losses added by the electrical circuit. By considering the damping parameter in the form $C_d = a\sqrt{P}$ where a is a parameter specific of the tuning fork, $Q(P)$ can be described as:

$$Q(P) = \frac{Q_0}{1 + Q_0 a\sqrt{P}} \quad (6)$$

2. Custom QTF characterization. By substituting the geometrical ($K = 0.375$ mm and $L = 17.7$ mm) and the elastic ($E = 0.72 \times 10^{11}$ N m^{-2}, the Young modulus of the quartz and $\rho = 2650$ Kg m^{-3} its density) parameters of the custom QTF in eqn (2), we obtain the first three solutions shown in Table 1. Note that $n = 0$ is ignored since it implies that the bar is at rest because $f_n = 0$. In Table 1 are also reported for comparison the f_n values calculated for a standard quartz tuning fork, having $L = 3.2$ mm and $K = 0.095$ mm.

Being a mechanical oscillator, the tuning fork can also be described in terms of an equivalent electrical series RLC circuit, where mass corresponds to inductance, rigidity to inverse capacity and damping to dynamic resistance R. To determine the quartz tuning fork parameters we used a control electronic unit (CEU) which measures the QTF resonant frequencies f_n, quality factor Q_n and the dynamic resistance R_n.

The CEU applies an ac voltage with variable frequencies to the QTF and records its piezoelectric response signal $I(f)$. In this way it determines the resonant frequencies f_n of the QTF and extract the corresponding quality factor $Q_n = f_n/\Delta f_n$, where Δf_n is the full-width-half-maximum of the $I(f_n)$ resonant band profile. The CEU has a high frequency cut-off of 50 kHz, thus we can measure only the first two resonant modes of the custom QTF.

In Fig. 2 are shown the $I(f)$ data relative to the observed two resonant modes at atmospheric pressure in pure N_2.

Resonance frequencies of $f_1 = 4.245$ kHz and $f_3 = 25.4$ kHz were measured and the corresponding quality factor Q_n and resistance R_n are: $Q_1 = 13\,100$, $R_1 = 6.5$ MΩ and $Q_3 = 9800$, $R_3 = 4.3$ MΩ. The discrepancies from the theoretical values, calculated under vacuum conditions (see Table 1), are due to damping effects of the ambient gas, additional weight of the electrode gold layers, dependence of the elasticity modulus of quartz on the crystallographic axis orientation and deviations in geometry between the modeled and the real QTF.

To study the damping effects induced by the environmental gas on the quality factor, we measured the $I(f)$ signal as a function of the gas pressure. Fig. 3 shows the resonant frequency f_1 and the Q_1 factor dependences as a function of the N_2 pressure. According to the prediction of eqn (5), f_1 shows a linear dependence of the gas pressure in the whole investigated range, with a slope of -1.19×10^{-3} Hz Torr^{-1}.

The intercept with the vertical axis at 4246.3 Hz gives the resonant frequency f_1 in a vacuum. A similar linear trend has been also observed for f_3 in the pressure range $10 \div 760$ Torr, with a slope of -4.49×10^{-3} Hz Torr^{-1} and an intercept with the vertical axis of 25 404.5 Hz. The Q_1 factor pressure dependence reported in Fig. 3(b) shows an exponential behavior, as predicted, and rapidly decreases with the gas pressure. The best fit parameters obtained using eqn (6) are: $a = 1.98 \times 10^{-6}$

Table 1 n values and the natural frequencies f_n for cantilever prong vibrations for the standard and the custom tuning fork employed in this work, calculated from eqn (2)

n	f_n (Hz) – standard tuning fork	f_n (Hz) – custom-made tuning fork
1.194	31 978	4118
2.988	200 263	25 786
5	560 764	72 204

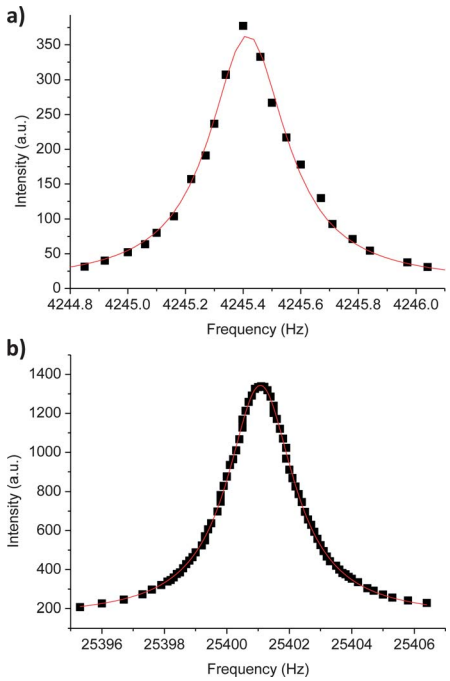

Fig. 2 QTF f_1 (panel a) and f_3 (panel b) frequency profiles measured at atmospheric pressure in pure N_2. The solid red lines are the Lorentzian best fits.

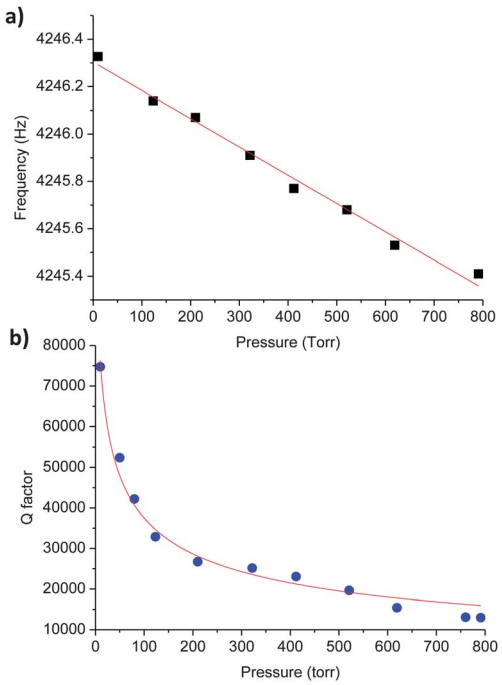

Fig. 3 (a) QTF resonance frequency f_1 measured as a function of the N_2 gas pressure (■). The red line is a linear fit of the data, (b) Q_1 factor measured as a function of the N_2 gas pressure (●). The red line is the best fit obtained using eqn (6).

Torr^{-1} and $Q_0 = 146\,350$. Similarly for Q_3 we observed an exponential pressure dependence and extracted the parameters: $a = 8.73 \times 10^{-7}\ \text{Torr}^{-1}$ and $Q_0 = 13\,180$.

The results obtained from the custom QTF characterization demonstrate that it behaves like a tuning fork resonator with Q_0 values similar to the standard one. Thus it can be employed for gas sensing applications in a QEPAS setup.

Experimental

A schematic of the gas sensor QEPAS setup is shown in Fig. 4.

The THz laser source employed in this work is a single-mode bound-to-continuum QCL emitting at 3.93 THz (~76.3 μm), driven in continuous wave (CW) mode and mounted on the cold finger of a continuous-flow cryostat equipped with polymethylpentene (TPX) windows. The operating heat sink temperature was 6 K.

The THz beam was focused between the two prongs of the tuning fork by using two 90° off-axis paraboloidal gold reflectors. The QTF is housed in an ADM with TPX input and output windows. The laser beam was recollimated upon exiting the ADM by means of a gold parabolic mirror. A reference cell (15 cm long) was filled with high concentration of the gas species under study for spectral reference. Another golden parabolic mirror was used to focus the laser beam exiting the reference cell to a pyroelectric detector. QCL wavelength locking function was performed using the 3f component of the pyroelectric detector output as the reference in a feedback algorithm.

In Fig. 5 is shown the 3D laser beam profile measured using a pyroelectric camera (mod. Spiricon Pyrocam III-C) on the focus plane of the ADM assembly, with the corresponding one-dimensional log-scale profile. From a Gaussian fit of the 2D beam profile (see Fig. 5(b)) we extracted a beam waist diameter of ~430 μm, well below the gap between the QTF prongs (~800 μm). Indeed, by measuring the radiation power transmitted through the QTF using a pyroelectric detector, we observed that almost 100% of the incoming laser beam was transmitted through the prongs, without being absorbed.

The lock-in amplifier (Stanford Research Model SR830) and the function generator (Tektronix model AFG3102) were controlled through a universal serial bus National Instruments card using Labview-based software. Unless differently specified, the lock-in time constant was set to 50 ms, corresponding to a

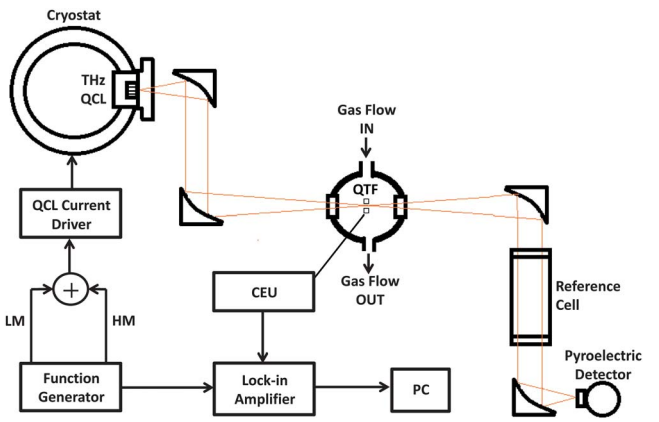

Fig. 4 Schematic of the QEPAS trace gas sensor using a THz QCL as an excitation source. CEU – Control Electronic Unit; LM – low-frequency modulation (triangular ramp); HM – sinusoidal high-frequency modulation; PC – personal computer.

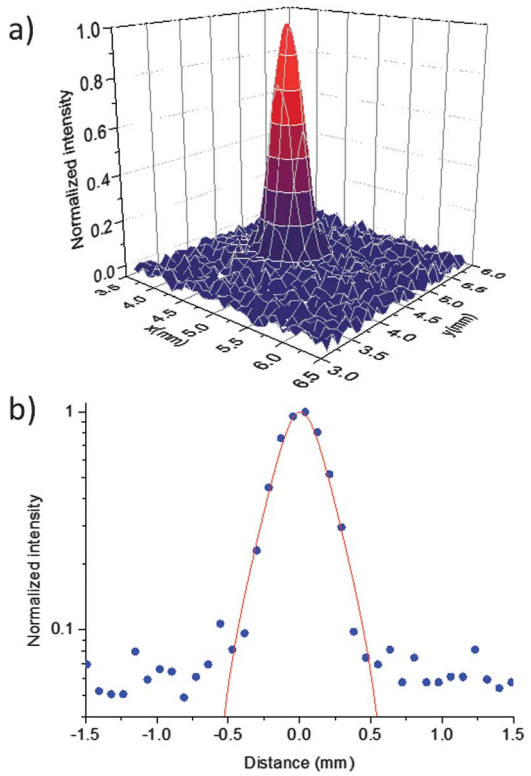

Fig. 5 (a) Three-dimensional beam profile of the THz-QCL at the focal point of the ADM assembly and (b) the corresponding two-dimensional profile on a log scale (●) and the related Gaussian fit (solid red line).

bandwidth of 3.335 Hz. QEPAS measurements were performed by applying a sinusoidal dither to the QCL current, while detecting the QTF response by means of the lock-in amplifier, after being amplified by a custom transimpedance amplifier with a feedback resistor of 10 MΩ and a gain factor of 30.

QEPAS 1f spectral measurements were performed by slowly scanning the laser wavelength over ~0.025 cm^{-1}, by means of a low-frequency (10 MHz) voltage ramp applied to the external analog modulation input of the QCL current supply (ILX-LDX 3232, bandwidth 0 Hz–250 kHz). A sinusoidal dither at f_n is contemporarily added to the low-frequency voltage ramp, to obtain up to 0.01 cm^{-1} optical frequency modulation.

The QEPAS 2f technique was implemented by applying a sinusoidal modulation to the QCL current at half of the QTF resonance frequency $f_n/2$ and detecting the QTF response at f_n. QEPAS 1f measurement in locked-mode was performed by keeping fixed the laser wavelength on the absorption peak frequency and modulating its current at f_n. Note that the changes in f_n due to pressure variation are of the same order of the resonance width Δf_n. Hence, neither precise pressure control, nor frequent and strong adjustments of the modulation frequency f_n during the experiments are needed.

For our THz QEPAS sensor demonstration we selected methanol as the target gas molecule. Methanol is widely used as a solvent, detergent or even denaturant additive for industrial ethanol. Methanol ingestion can be fatal due to its toxication by the alcohol dehydrogenase in the liver, by forming formic acid and formaldehyde. The selected methanol absorption line was the $(v = 1, K = 6, J = 11) \leftarrow (1, 5, 10)$ rotational translational transition, falling at $\nu_{line} = 3.9289$ THz (131.054 cm^{-1}) with line-strength $S = 4.28 \times 10^{-21}$ cm mol^{-1} in HITRAN units.[30,31] In the laser emission range the selected absorption line is about two orders of magnitude stronger than that of the nearby methanol absorption lines. So absorption measurements using the reference cell allow us to fine tune the laser frequency on the selected methanol absorption line.

1. QEPAS signal analysis

In QEPAS spectral measurements, the voltage ramp slowly scans the laser wavelength through the absorption feature for a line-shape interrogation, while the sinusoidal current dither generates a frequency modulation of amplitude $\Delta\nu$, through the tuning rate of the laser. In Fig. 6 are shown the QEPAS 1f (S_{1f}) and 2f (S_{2f}) spectral signals obtained at f_1 and 10 Torr, for a gas mixture containing 0.4% methanol in N_2. With a pressure broadening coefficient of 10 MHz $Torr^{-1}$ the expected line-width is $\Delta\nu_{line} \sim 100$ MHz (half width at half maximum, HWHM),[32] with a negligible Doppler contribution (4.5 MHz HWHM). We used this estimate to convert the horizontal scale in Fig. 6 from time to frequency detuning (MHz). Here, $x = (\nu - \nu_{line})/\Delta\nu_{line}$ and $m = \Delta\nu/\Delta\nu_{line}$ is the modulation index.

Differently from what expected, the QEPAS 1f spectra signal does not show the 1st derivative-like form (see Fig. 6(a)), but has the line-shape typical of a direct absorption signal. Correspondingly, the QEPAS 2f spectrum (see Fig. 6(b)) does not have a pure 2nd derivative line-shape, but is slightly distorted. This distortion is manifested in particular through an asymmetry on both sides of the spectrum around the peak. We observed that

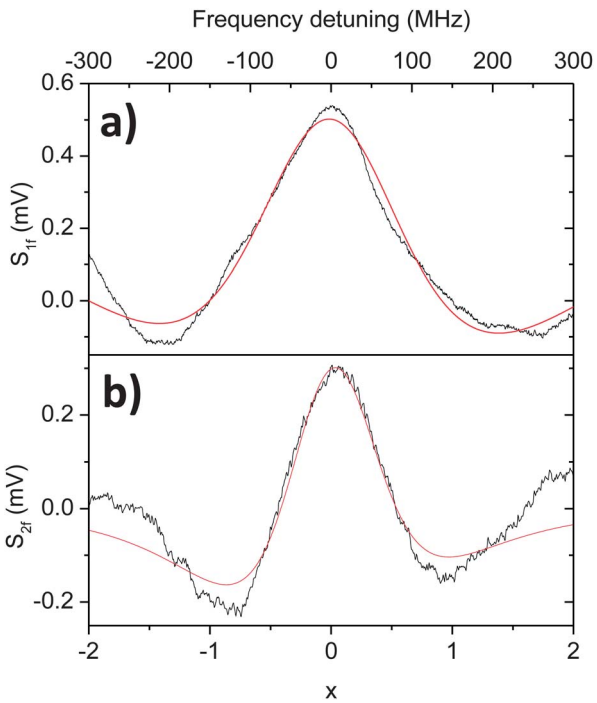

Fig. 6 QEPAS 1f (panel a) and 2f (panel b) signals obtained for a gas mixture containing 0.4% of methanol in N_2 at 10 Torr. The red lines are simulated signals as reported in the text.

this signal asymmetry increases with the current modulation intensity and also depends on the selected lock-in detection phase. These behaviors can be explained, if one considers that, differently from mid-IR QCL sources, where modulations of the laser frequency across the selected absorption band require a small laser current excursion, THz QCLs are characterized by a much smaller wavelength tunability, thus to scan across the absorption line a much stronger current variation is required, both for scanning and modulation purposes. As a consequence, together with the wavelength modulation effect a strong amplitude modulation influence has to be expected.

A detailed QEPAS signal analysis will require a complex theoretical treatment, which is beyond the scope of the present work. However, the following simplified analysis is able to qualitative describe the observed behaviour. If one considers the instantaneous laser frequency as: $\nu(t) = \nu_0 - \Delta\nu \cos(2\pi ft)$ where ν_0 is the optical carrier frequency and f is the laser injected current modulation frequency, the current waveform applied to the QCL produces a variation of the laser intensity given by $I(t) = I_0 + \Delta I \cos(2\pi ft)$. The amplitude ΔI of the sinusoidal intensity modulation is determined by the slope of the laser power *versus* current characteristics, which can be assumed constant across the scan.[33] According to the Beer's law and assuming small light absorptions, we can expand in Taylor's series the absorption coefficient $\alpha(\nu)$, considering small $\Delta\nu$ and neglecting the phase shift between the power and the frequency modulation. The absorbed intensity among the prongs of thickness T results:

$$I_{abs}(t) = [I_0 + \Delta I \cos(2\pi ft)]\left[1 - T\left(\alpha_0 + \left.\frac{\partial\alpha}{\partial\nu}\right|_{\nu=\nu_0}\Delta\nu\cos(2\pi ft) + \frac{1}{2}\left.\frac{\partial^2\alpha}{\partial\nu^2}\right|_{\nu=\nu_0}(\Delta\nu)^2\cos^2(2\pi ft)\right)\right] \quad (7)$$

where α_0 is the background absorption. Considering the trigonometric identity $\cos^2(2\pi ft) = 1/2 + 1/2\cos(4\pi ft)$, the 2f harmonic terms result proportional to $\partial^2\alpha/\partial^2\nu$. This demonstrates that the background absorption contributes only to the S_{1f} signal, whereas it does not contribute to the S_{2f} one. Analytically, if we assume that the absorption coefficient has a pure Lorentzian lineshape with amplitude η, S_{1f} has the form:

$$S_{1f} = \Delta I(1 - T\alpha_0) + 8\eta m\left(\frac{I_0 x}{(4x^2+1)^2}\right) \quad (8)$$

Assuming that I_0 varies linearly during the voltage ramp, *i.e.* $I_0 \rightarrow I_0 + I_{ramp}x$, S_{1f} becomes:

$$S_{1f} = \Delta I(1 - T\alpha_0) + 8\eta m\left[\frac{I_0 x}{(4x^2+1)^2} + \frac{I_{ramp}x^2}{(4x^2+1)^2}\right] \quad (9)$$

The first term, is related to the background absorption, the second term is proportional to the absorption first derivative, whereas the last term is the contribution due to the laser intensity variation during the spectral scan. With the same assumption, the S_{2f} signal has the form:

$$S_{2f} = 8\eta m\left[\frac{\Delta I x}{(4x^2+1)^2} - \frac{1}{2}I_0 m\left[\frac{12x^2-1}{(4x^2+1)^3}\right] - \frac{1}{2}I_{ramp}m\left[\frac{12x^3-x}{(4x^2+1)^3}\right]\right] \quad (10)$$

Correspondingly, the first term, arising from the residual amplitude modulation, is proportional to the first derivative, whereas the second one is the usual 2nd-derivative term arising from the laser wavelength modulation and the last term is the contribution due to the laser intensity variation. In Fig. 6 are shown two calculated S_{1f} and S_{2f} spectra, qualitatively reproducing the lineshape of the measured corresponding signals. For our simulations we used the experimentally measured I_0, I_{ramp} and m.[33] Our results demonstrate that the effect of a non-negligible amplitude modulation in QEPAS spectral scan measurements gives rise to significant signal distortions.

From eqn (9) and (10) we assert that the 2f detection has the advantage of minimizing the background caused by the spectrally non-selective absorption of stray radiation α_0. However, we found that the S_{1f} background signal is stable over at least one hour and this permits an efficient background subtraction. Moreover, the signal-to-noise ratio measured in QEPAS 1f experiments results ~4 times larger than that observed in QEPAS 2f, thus for the sensor operation we selected the QEPAS 1f configuration. The S_{1f} background signal was separately recorded when fluxing pure N_2 in the ADM and subsequently subtracted from the total measured signal.

To find the optimal operating conditions in terms of QEPAS signal-to-noise ratio, we investigated the effects of gas pressure and modulation amplitude. The gas pressure influences the QEPAS signal mostly because the Q-factor decreases at higher pressures, while the rotational–translational (R–T) energy transfer relaxation rate is faster at higher pressures, resulting in more efficient sound production.[34] It is important to underline that, in standard QTF, the third flexural mode falls at frequencies >200 kHz, which prevent its use for QEPAS sensing, since it requires too fast gas energy relaxation times and thus cannot be taken into account for spectroscopic applications. Differently, the employed custom QTF makes it possible to use both the resonances, thus extending the capabilities of the developed QEPAS THz system.

In order to determine the optimal sensor working parameter, we measured the QEPAS signal as a function of the resonance mode, the gas pressure and the laser modulation amplitude. In Fig. 7 is shown the S_{1f} peak signal as a function of gas pressure for both QTF resonance frequencies. The S_{1f} peak signals for the two resonances have been normalized to the related obtained maximum value. The measurements were carried out using a 1% methanol in a N_2 gas mixture, operating in locked mode.

As can be expected, the low frequency resonance f_1 shows a maximum value at lower pressure (10 Torr), with respect to f_3 (45 Torr). This behaviour can be explained considering that operating at lower frequency partially relaxes the requirement of fast energy R–T relaxation rates, allowing to work at low gas pressure, so taking advantage of the corresponding exponential increase of the Q-factor. Indeed, we measured $Q_1 = 76\,300$ at 10 Torr and $Q_3 = 12\,250$ at 45 Torr.

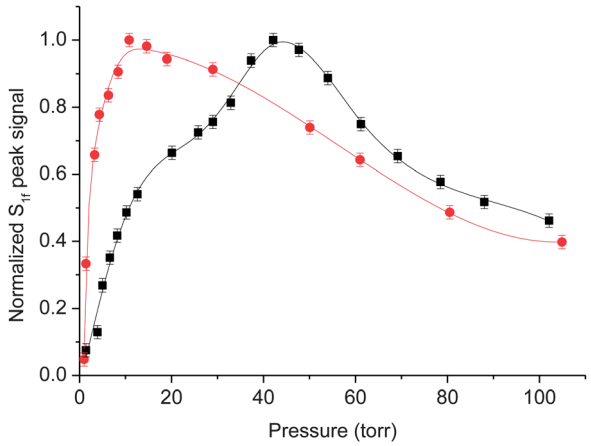

Fig. 7 Plot of normalized QEPAS S_{1f} peak signal as a function of the gas mixture pressure for f_1 (●) and f_3 (■) QTF resonances. The solid lines are guides for the eye.

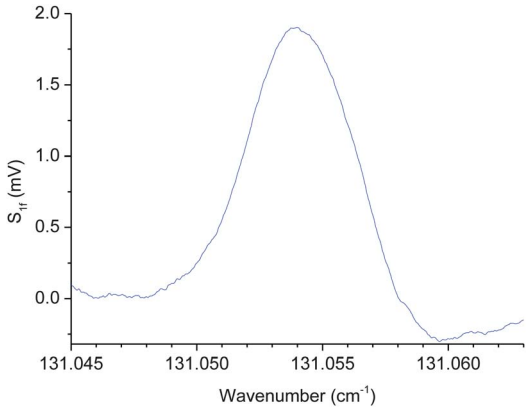

Fig. 9 QEPAS S_{1f} spectral scan of a gas mixture containing 1.55% methanol in N_2 at $P = 10$ Torr, acquired with 1 second lock-in integration time.

Correspondingly, at the same methanol concentration the S_{1f} peak signal measured at f_1 and a pressure of 10 Torr results ~30 times higher than the peak value recorded at f_3 and 45 Torr. For all these reasons we selected the first flexion mode for the sensor operation.

To select the optimal laser modulation factor, we performed QEPAS experiments in scan mode, by applying a sinusoidal voltage signal at f_1 to the laser driver in the range of 200–800 mV. In Fig. 8 are reported two representative curves showing the S_{1f} peak values *versus* the methanol concentration obtained at 600 mV and 400 mV. The optimal sensor operating conditions were found to occur at a modulation amplitude of 600 mV (see the inset of Fig. 7). In all the investigated laser modulation ranges a good linearity of the QEPAS sensor *versus* the methanol concentration has been observed. Thus, to summarize, the optimal sensor operating conditions were found to occur at f_1, a gas pressure of 10 Torr and a modulation amplitude of 600 mV.

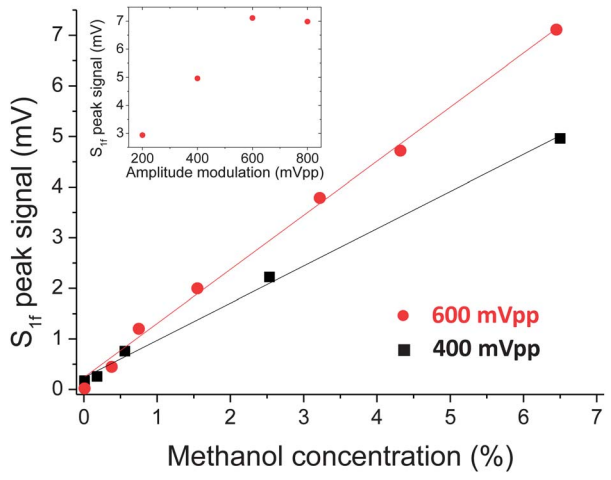

Fig. 8 Plot of the QEPAS S_{1f} peak signal intensity as a function of the methanol concentration for f_1 at laser modulation voltages of 400 mV (■) and 600 mV (●). The solid lines are the best linear fits. The S_{1f} background signals were subtracted from the total measured signal. Inset: S_{1f} peak signal intensity at four different modulation amplitude values referred to a methanol concentration of 6.5%.

2. Methanol concentration measurements

In Fig. 9 is shown a representative QEPAS 1f scan measured at 1.55% methanol concentration, at 10 Torr and lock-in integration time of 1 second. No fringe-like interference patterns are visible, proving that a negligible portion of the THz optical power is absorbed by the ADM. From the analysis of the signal-to-noise ratio we extract a 1σ detection limit of 45 ppm.

Stepwise concentration measurements at 10 Torr were performed to verify the linearity of S_{1f} as a function of the methanol concentration. The system was operating in the locked mode, *i.e.* with the laser frequency set to the center of the selected methanol absorption line. Under this condition an optical laser power of 40 μW is measured between the two prongs of the QTF by means of a calibrated pyroelectric detector.

The gas concentrations have been varied by diluting methanol vapors with pressurized N_2. A certified 100 ppm methanol/N_2 gas mixture has been also employed.[26] The obtained results are shown in Fig. 10.

The S_{1f} signal for each concentration step was measured every 100 ms, for a total time duration of more than 10 minutes. In order to allow the gas mixture concentration to stabilize, we stopped the signal acquisition for 30 seconds when we changed the methanol concentration. Data for each step were averaged and a calibration curve was obtained (the inset of Fig. 10). The results confirm that the QEPAS signal is proportional to the methanol concentration. Note that the QTF thermal noise is 0.12 μV, several times smaller than the measured one,[26] meaning that the sensor detection is mostly limited by the stability of the laser source. To determine the best achievable sensitivity of the QEPAS sensor we performed an Allan variance analysis, measuring and averaging the QEPAS signal.[26] For a 4 second averaging time we extracted a minimum detection sensitivity of 7 ppm, corresponding to a NNEA $= 2 \times 10^{-10}$ cm^{-1} W $Hz^{-1/2}$, comparable with the best result obtained in the mid-IR.[22,35]

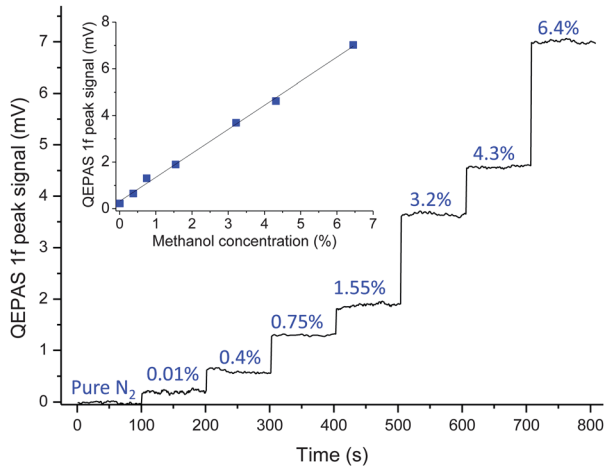

Fig. 10 Stepwise measurements at 10 Torr pressure obtained at different methanol concentrations. Inset: calibration curve obtained from the measured S_{1f} peak signals (■) and corresponding methanol concentrations. The solid line is the best linear fit. The S_{1f} background signal was subtracted from the total measured signal.

Conclusions

We demonstrate the possibility of extending the QEPAS technique in the THz spectral range, employing custom QTFs. Since rotational levels are involved in THz absorption processes and are characterized by fast relaxation rates, this allows operation at low gas pressure gaining in high QTF *Q*-factors (several tens of thousands) and selectivity of the QEPAS sensor system. Moreover, the employed custom QTF makes it possible to work on different resonance modes, extending the capabilities of the QEPAS THz system. Indeed, the use of the third flexion resonance at ~25 kHz is advantageous in terms of white noise reduction and can be selected when dealing with fast relaxing gases, while the first flexion resonance at ~4 kHz has to be preferred when dealing with slowly relaxing molecules, such as CO or NO.[25]

The independence of the QTF transducer from the laser wavelength makes the QEPAS sensors highly versatile, leading to the possibility of investigating different spectral ranges, by simply substituting the source. In particular, the use of state of art THz QCLs with >100 mW emission power[12] would allow the detection of molecules such as HF, H_2S, OH, NH_3, HCN, *etc.*, having absorption strengths larger than 10^{-19} cm mol^{-1}, down to the parts per trillion concentration range.

Finally, since the geometry of the QTF employed to date in QEPAS systems have been optimized only in terms of resonance frequency, *i.e.* for timing applications, the possibility to realize QTFs of improved geometry in terms of sensing performances may further enhance the QEPAS detection capability.

Acknowledgements

The authors acknowledge financial support from the Italian national projects: PON01_02238, PON02_00675 and PON02_00576. We thank A. Tredicucci for fruitful interactions, F. Tittel for helpful discussions, A. Kachanov for providing the custom quartz tuning fork and P. P. Calabrese for realizing the fork housing. M.S.V. acknowledge financial support of the Italian Ministry of Education, University, and Research (MIUR) through the program "FIRB-Futuro in Ricerca 2010" RBFR10LULP "Fundamental research on terahertz photonic devices".

References

1 J. W. Waters, *IEEE Trans. Geosci. Electron.*, 2006, **44**, 1075–1092.
2 P. De Natale, L. Lorini, M. Inguscio, I. G. Nolt, J. H. Park, G. Di Lonardo, L. Fusina, P. A. R. Ade and A. G. Murray, *Appl. Opt.*, 1997, **36**, 8526–8532.
3 M. Bellini, P. De Natale, G. Di Lonardo, L. Fusina, M. Inguscio and M. Prevedelli, *J. Mol. Spectrosc.*, 1992, **152**, 256–259.
4 M. R. Leahy-Hoppa, M. J. Fitch, X. Zheng, L. M. Hayden and R. Osiander, *Chem. Phys. Lett.*, 2007, **434**, 227–230.
5 M. Lu, J. Shen, N. Li, Y. Zhang, C. Zhang, L. Liang and X. Xu, *J. Appl. Phys.*, 2006, **100**, 103104.
6 D. Bigourd, A. Cuisset, F. Hindle, S. Matton, R. Bocquet, G. Mouret, F. Cazier, D. Dewaele and H. Nouali, *Appl. Phys. B*, 2007, **86**, 579–586.
7 E. Gerecht, K. O. Douglass and D. F. Plusquellic, *Opt. Express*, 2011, **19**, 8973–8984.
8 S. A. Harmon and R. A. Cheville, *Appl. Phys. Lett.*, 2004, **85**, 2128–2130.
9 R. Kohler, A. Tredicucci, F. Beltram, H. E. Beere, E. H. Linfield, A. G. Davies, D. A. Ritchie, R. C. Iotti and F. Rossi, *Nature*, 2002, **417**, 156–159.
10 B. S. Williams, *Nat. Photonics*, 2007, **1**, 517–525.
11 M. S. Vitiello and A. Tredicucci, *IEEE Trans. Terahertz Sci. Technol.*, 2011, **1**, 76–84.
12 B. S. Williams, S. Kumar, Q. Hu and J. L. Reno, *Electron. Lett.*, 2006, **42**, 89–90.
13 M. S. Vitiello, L. Consolino, S. Bartalini, A. Taschin, A. Tredicucci, M. Inguscio and P. De Natale, *Nat. Photonics*, 2012, **6**, 525–528.
14 H. W. Hübers, M. F. Kimmitt, N. Hiromoto and E. Brundermann, *IEEE Trans. Terahertz Sci. Technol.*, 2011, **1**, 321–331.
15 Y. Ren, D. J. Hayton, J. N. Hovenier, M. Cui, J. R. Gao, T. M. Klapwijk, S. C. Shi, T.-Y. Kao, Q. Hu and J. L. Reno, *Appl. Phys. Lett.*, 2012, **101**, 101111.
16 L. Consolino, S. Bartalini, H. E. Beere, D. A. Ritchie, M. S. Vitiello and P. De Natale, *Sensors*, 2013, **13**, 3331–3340.
17 A. Elia, P. M. Lugarà, C. Di Franco and V. Spagnolo, *Sensors*, 2009, **9**, 9616–9628.
18 A. A. Kosterev, F. K. Tittel, D. V. Serebryakov, A. L. Malinovsky and I. V. Morozov, *Rev. Sci. Instrum.*, 2005, **76**, 043105.
19 L. Dong, A. A. Kosterev, D. Thomazy and F. K. Tittel, *Appl. Phys. B*, 2010, **100**, 627–635.
20 K. Liu, H. Yi, A. A. Kosterev, W. Chen, L. Dong, L. Wang, T. Tan, W. Zhang, F. K. Tittel and X. Gao, *Rev. Sci. Instrum.*, 2010, **81**, 103103.

21 L. Dong, V. Spagnolo, R. Lewicki and F. K. Tittel, *Opt. Express*, 2011, **19**, 24037–24045.
22 V. Spagnolo, P. Patimisco, S. Borri, G. Scamarcio, B. E. Bernacki and J. Kriesel, *Opt. Lett.*, 2012, **37**, 4461–4463.
23 J. Hodgkinson and R. P. Tatam, *Meas. Sci. Technol.*, 2013, **24**, 012004.
24 W. H. Flygare, *Acc. Chem. Res.*, 1968, **1**, 121–127.
25 V. Spagnolo, A. A. Kosterev, L. Dong, R. Lewicki and F. K. Tittel, *Appl. Phys. B*, 2010, **100**, 125–130.
26 S. Borri, P. Patimisco, A. Sampaolo, M. S. Vitiello, H. E. Beere, D. A. Ritchie, G. Scamarcio and V. Spagnolo, *Appl. Phys. Lett.*, 2013, **103**, 021105.
27 S. Lee, J. Y. Lee and T.-S. Park, *Mater. Corros.*, 2001, **52**, 712–715.
28 M. Christen, *Sens. Actuators*, 1983, **4**, 555–554.
29 W. Zhang and K. Turner, *Sens. Actuators, A*, 2007, **134**, 594–599.
30 G. Moruzzi, P. Riminucci, F. Strumia, B. Carli, M. Carlotti, R. M. Lees, I. Mukhopadhyay, J. W. C. Johns, B. P. Winnewisser and M. Winnewisser, *J. Mol. Spectrosc.*, 1990, **144**, 139–200.
31 H. M. Pickett, R. L. Poynter, E. A. Cohen, M. L. Delitsky, J. C. Pearson and H. S. P. Muller, *J. Quant. Spectrosc. Radiat. Transfer*, 1998, **60**, 883–890.
32 Y. Ren, J. N. Hovenier, R. Higgins, J. R. Gao, T. M. Klapwijk, S. C. Shi, A. Bell, B. Klein, B. S. Williams, S. Kumar, Q. Hu and J. L. Reno, *Appl. Phys. Lett.*, 2010, **97**, 161105.
33 T. Losco, J. H. Xu, R. P. Green, A. Tredicucci, H. E. Beere and D. A. Ritchie, *Physica E*, 2008, **40**, 2207–2209.
34 A. A. Kosterev, F. K. Tittel, D. V. Serebryakov, A. L. Malinovsky and I. V. Morozov, *Rev. Sci. Instrum.*, 2005, **76**, 043105.
35 V. Spagnolo, P. Patimisco, S. Borri, G. Scamarcio, B. E. Bernacki and J. Kriesel, *Appl. Phys. B*, 2013, **112**, 25–33.